Ultrasound in Med. & Biol., Vol. 00, No. 00, pp. 1−17, 2019

0301-5629/$ - see front matter

https://doi.org/10.1016/j.ultrasmedbio.2019.09.010

● *Original Contribution*

A CLINICAL SYSTEM FOR NON-INVASIVE BLOOD−BRAIN BARRIER OPENING USING A NEURONAVIGATION-GUIDED SINGLE-ELEMENT FOCUSED ULTRASOUND TRANSDUCER

Antonios N. Pouliopoulos,* Shih-Ying Wu,* Mark T. Burgess,* Maria Eleni Karakatsani,*
Hermes A.S. Kamimura,* and Elisa E. Konofagou*,†
* Department of Biomedical Engineering, Columbia University, New York City, New York, USA; and † Department of Radiology, Columbia University, New York City, New York, USA

(*Received* 29 *July* 2019; *revised* 16 *September* 2019; *in final from* 16 *September* 2019)

Abstract—Focused ultrasound (FUS)-mediated blood-brain barrier (BBB) opening is currently being investigated in clinical trials. Here, we describe a portable clinical system with a therapeutic transducer suitable for humans, which eliminates the need for in-line magnetic resonance imaging (MRI) guidance. A neuronavigation-guided 0.25-MHz single-element FUS transducer was developed for non-invasive clinical BBB opening. Numerical simulations and experiments were performed to determine the characteristics of the FUS beam within a human skull. We also validated the feasibility of BBB opening obtained with this system in two non-human primates using U.S. Food and Drug Administration (FDA)-approved treatment parameters. Ultrasound propagation through a human skull fragment caused 44.4 ± 1% pressure attenuation at a normal incidence angle, while the focal size decreased by 3.3 ± 1.4% and 3.9 ± 1.8% along the lateral and axial dimension, respectively. Measured lateral and axial shifts were 0.5 ± 0.4 mm and 2.1 ± 1.1 mm, while simulated shifts were 0.1 ± 0.2 mm and 6.1 ± 2.4 mm, respectively. A 1.5-MHz passive cavitation detector transcranially detected cavitation signals of Definity microbubbles flowing through a vessel-mimicking phantom. T_1-weighted MRI confirmed a 153 ± 5.5 mm^3 BBB opening in two non-human primates at a mechanical index of 0.4, using Definity microbubbles at the FDA-approved dose for imaging applications, without edema or hemorrhage. In conclusion, we developed a portable system for non-invasive BBB opening in humans, which can be achieved at clinically relevant ultrasound exposures without the need for in-line MRI guidance. The proposed FUS system may accelerate the adoption of non-invasive FUS-mediated therapies due to its fast application, low cost and portability. (E-mail: ek2191@columbia.edu) © 2019 World Federation for Ultrasound in Medicine & Biology. All rights reserved.

Key Words: **Blood−brain barrier, Focused ultrasound, Clinical system, Drug delivery.**

INTRODUCTION

Focused ultrasound (FUS) serves as a non-invasive and non-ionizing therapeutic modality, with applications in lithotripsy (Miller and Thomas 1996), tumor ablation (Xia et al. 2012), neuromodulation (Kamimura et al. 2016; Tyler et al. 2018) and essential tremor treatment (Lipsman et al. 2013; Elias et al. 2016). Microbubbles are routinely used as contrast agents in ultrasound imaging (Cosgrove and Harvey 2009) and as stress mediators in ultrasound therapy (Coussios and Roy 2008) to deliver drugs into cells (Fan et al. 2012; Shamout et al. 2015), tumors (Graham et al. 2014; Sun et al. 2017; Arvanitis et al. 2018) or tissues (Kotopoulis et al. 2013). In conjunction with systemically circulating microbubbles, FUS can perform targeted, non-invasive and reversible blood−brain barrier (BBB) opening (Hynynen et al. 2001; Konofagou 2012). FUS-mediated BBB opening has been successfully and safely tested for well over 15 years in a variety of animal models, from rodents (Choi et al. 2007; Sheikov et al. 2008) to non-human primates (NHPs) (Marquet et al. 2011; Arvanitis et al. 2012; Wu et al. 2018). The success of these preclinical studies has paved the way toward clinical implementation of this technology.

The first published clinical study regarding the application of ultrasound and microbubbles to increase BBB permeability was reported by Carpentier et al. (2016). The authors used an implantable 11.5-mm unfocused single-element 1.05-MHz transducer called SonoCloud (Goldwirt et al. 2016; Horodyckid et al. 2017), which was fixed within the skull bone and connected to an external power

---

Address correspondence to: Elisa E. Konofagou, 351 Engineering Terrace, 1210 Amsterdam Avenue, Mail Code: 8904, New York, NY 10027, USA. E-mail: ek2191@columbia.edu

supply via a transdermal needle. Glioblastoma multiforme (GBM) patients were enrolled in this study and were exposed to repeated monthly FUS treatments before receiving systemic chemotherapy with carboplatin. The results indicated that the BBB was disrupted at acoustic pressures up to 1.1 MPa (*i.e.,* mechanical index [MI] = 1.07) without detectable adverse effects on magnetic resonance imaging (MRI) or clinical examination. Results from a larger cohort of 19 subjects revealed an increase in median progression-free survival for patients with clear BBB disruption (Idbaih et al. 2019). The same group has developed a quantification method for FUS treatment assessment (Asquier et al. 2019) and is conducting a clinical trial with Alzheimer's disease (AD) patients (NCT03119961). In addition, GBM patients are currently treated with a new-generation SonoCloud, which enlarges the treatment volume by nine times (SC9; NCT03744026); this device has recently received U.S. Food and Drug Administration (FDA) approval for a phase 1/2a trial in the United States.

Another non-invasive approach involves the generation of FUS through a 1024-element 0.22-MHz hemispherical array embedded within the MRI bore. Real-time acoustic emission monitoring is used to determine the pressure levels during the FUS treatment (O'Reilly and Hynynen 2012). The first study revealing BBB opening in 5 AD patients using the MR-guided ExAblate system developed by Insightec (Insightec Inc., Tirat Carmel, Israel) was published by Lipsman et al. (2018). AD patients received FUS treatments aimed at the dorsolateral prefrontal cortex. BBB opening was fully reversible, with no contrast enhancement detected 1d after treatment. The same group recently published results from a trial with a cohort of five GBM patients, who have been treated with FUS in combination with temozolomide or doxorubicin (Mainprize et al. 2019). BBB opening was observed in all patients and an increase of the delivered chemotherapy was measured in the 2 patients for whom data were available. Currently, there are multiple clinical trials using the ExAblate Neuro system throughout the world, for targeted BBB opening in patients with GBM (NCT03322813, NCT03712293, NCT03616860, NCT03551249); AD (NCT02986932, NCT03671889, NCT03739905), Her2-positive breast cancer brain metastases (NCT03714243); amyotrophic lateral sclerosis (NCT03321487); and Parkinson's disease (PD) dementia (NCT03608553). Among the advantages of multi-element arrays are the ability to correct for skull-induced aberrations based on computed tomography (CT) scans of the treated subject (Clement and Hynynen 2002; Aubry et al. 2003), simultaneous treatment monitoring via passive cavitation mapping (Jones et al. 2013), standing wave reduction and flexibility in the positioning of the focal volume through electronic steering.

An alternative approach is to employ neuronavigation systems instead of MRI for FUS guidance. Neuronavigation-assisted BBB opening using a 0.4-MHz single-element transducer was proposed by Wei et al. (2013). It was found that the precision of this technique was comparable to that of stereotactic procedures in a swine model, with a targeting error of 2.3 ± 0.9 mm. BBB opening was observed above a derated pressure threshold of 0.43 MPa at 0.4 MHz (*i.e.,* MI = 0.68), using a constant infusion of 0.3 mL/kg/min SonoVue microbubbles. Clinical trials with this system, called NaviFUS, are currently in progress in Taiwan, recruiting GBM (NCT03626896) and drug-resistant epilepsy (NCT03860298) patients.

Our group has reported on successful BBB opening through neuronavigation targeting in an NHP model with simultaneous real-time passive cavitation detection (PCD) and passive acoustic mapping (PAM) (Wu et al. 2018). In this study, the average precision between planned and actual targeting was 3.1 mm, compared with 4.3 mm for the frame-based stereotaxis. The BBB opening threshold was 350 kPa at 0.5 MHz (MI = 0.5), using 4- to 5-μm monodisperse microbubbles at a dose of 2.5×10^8 microbubbles/kg. We found that 2-D PAM can be used to predict and verify the BBB opening location. The total FUS procedure duration was less than 30 min, which is equivalent to the duration of standard radiation therapy.

Here, we sought to establish the clinical relevance of the previously described approach and develop a neuronavigation-guided focused ultrasound (NgFUS) system suitable for use in humans. Our objectives were to (i) perform BBB opening at a lower frequency of 0.25 MHz, which would allow for lower attenuation/distortion of the ultrasound beam and would thus be more suitable for humans; (ii) determine the transducer characteristics (*e.g.,* radius of curvature and aperture size) required to expand the treatment envelope and enable coverage of the human brain using a single-element FUS transducer; (iii) confirm the ability of low-frequency PCD transducers to detect cavitation signals through the human skull; and (iv) investigate whether BBB opening with real-time PCD monitoring is possible in an NHP model using Definity microbubbles at the FDA-approved dose for ultrasound imaging applications and clinically relevant ultrasound parameters. The same system is currently being designated for testing in a small cohort of AD subjects.

METHODS

Numerical simulations

Numerical simulations of ultrasound propagation through the human skull were performed in two dimensions using the k-Wave acoustics toolbox (Treeby and

Table 1. Transducer parameters used in numerical simulations

Transducer	Center frequency (MHz)	Outer diameter (mm)	Inner diameter (mm)	Radius of curvature (mm)
1	0.2	110	44	70
2	0.35	60	44	76
3	0.25	110	44	110

Cox 2010; Treeby et al. 2012), to test different transducer characteristics. We first investigated the trade-off between the focal depth and aperture size, that is, the *f*-number, within the human skull. Our aim was to determine the center frequency, outer diameter and radius of curvature, to be able to target both cortical and subcortical regions of the human brain, thus enlarging the treatment envelope. We tested three different transducer configurations (Table 1) based on commercially available low-frequency models (transducer 1: Sonic Concepts H-149, transducer 2: Sonic Concepts H-209) and a custom-designed transducer (transducer 3). H-149 and H-209 were commercially available models that we identified as potentially appropriate for BBB opening applications in humans. These transducers were chosen as examples of small and large *f*-number, respectively (0.64 vs. 1.27). The custom-designed transducer (outer diameter: 110 mm, radius of curvature: 110 mm, *f*-number: 1) was optimized after multiple iterations of different designs, with emphasis on the outer diameter (search space: 60−140 mm) and radius of curvature (search space: 70−120 mm). To allow for insertion of a PCD transducer or a receiving ultrasound array, an inner gap 44 mm in diameter was applied in all transducer designs.

A human CT skull DICOM file from the Cancer Imaging Archive (2017; Head−Neck Cetuximab demo) was used as input in our simulations. Hounsfield CT units were converted to sound speed and medium density, as described previously (Aubry et al. 2003; Wu et al. 2018). Sound speed, medium density and attenuation coefficient within the brain were set to be equal to those of water at 37°C (*i.e.,* 1524 m/s, 1000 kg/m^3 and 3.5×10^{-4} dB/MHz·cm, respectively). The transducers were positioned close to the skull in an effort to place the focal volume as close to the brain median plane as possible, while maintaining a reasonable radius of curvature and realistic housing dimensions (Table 1). A number of axial offsets were tested (range: −30 to +30 mm, step 10 mm), to determine the evolution of focal shifts across different depths. In the case of an axial offset of 0 mm, the transducer's nominal focus was positioned at the human brain midline. The primary aim of these simulations was to evaluate the effect of different focusing depths on the focal volume distortion; therefore, we tested only axial offsets and not lateral offsets. Introducing lateral offsets would produce a large variation in the incidence angle, deviating significantly from the desirable 90^o incidence. Therefore, the lateral position of the FUS transducer center was fixed at $y = 0$ mm for all simulations. We have also tested pulses of different lengths (*i.e.,* 1, 5, 25 and 2500 cycles) to investigate the effects of interference and standing waves within the human skull. To calculate the theoretical ultrasound transmission coefficient through the human skull, we repeated the simulations with different pulse lengths in free field by replacing the human skull with water. The simulation grid was equal to 300 × 300 mm, at 1-mm spatial resolution, while the temporal resolution was 143 ns with a total of 7000 time steps or exposure time of 1 ms. For the pulse length of 2500 cycles, the simulation consisted of 70,000 time steps or 10 ms, to enable comparison with the treatment scheme typically used for *in vivo* BBB opening. Shear waves were not taken into account in these simulations. Axial (*i.e.,* x) and lateral (*i.e.,* y) axes were defined with respect to the FUS transducer, and had left to right and anterior to posterior directions, respectively.

Clinical system description

In the proposed clinical system (Fig. 1), we chose a low center frequency (*i.e.,* 0.25 MHz) to reduce the attenuation caused by the human skull and decrease the pressure threshold for cavitation induction (Apfel and Holland 1991). The first step was to refine the dimensions and characteristics of the single-element spherical-segment transducer based on numerical simulations. We then constructed the chosen single-element FUS transducer (Part No. H-231, center frequency: 0.25 MHz; Sonic Concepts, Bothell, WA, USA) and attached it onto a robotic arm (Kinova Jaco^2, Kinova, Boisbriand, QC, Canada). The robotic arm had 4 degrees of freedom and a maximum midrange loading capacity of 4.4 kg, and was controlled via a joystick. The whole construct was fixed onto a wheeled cart, making the system portable to any location.

The clinical FUS transducer was driven by a function generator (33500B Series, Agilent Technologies, Santa Clara, CA, USA) through a 55-dB radiofrequency power amplifier (A150, E&I, Rochester, NY, USA) using clinically relevant parameters (Table 2). A water degassing system (WDS105+, Sonic Concepts) was used to fill the transducer cone with degassed water and inflate or deflate the cone according to the sonicated location. Reflective beads were attached to the transducer to enable real-time tracking of its location through an infrared camera acting as a position sensor and neuronavigation guidance (BrainSight; Rogue Research, Montreal, QC, Canada). Using the bull's eye view function, we have previously shown high targeting accuracy with spatial error lower than 2 mm (Wu et al. 2018).

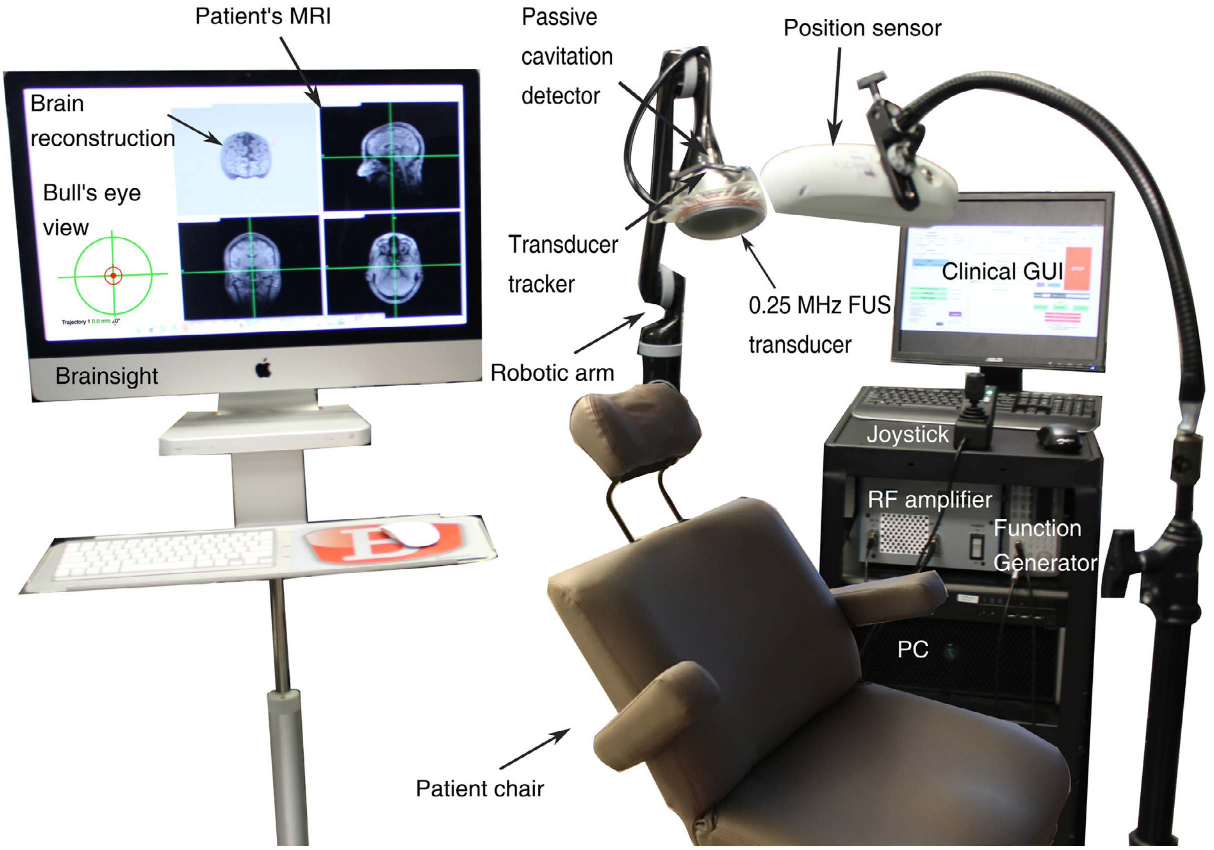

Fig. 1. Clinical setup with a single-element transducer and neuronavigation guidance. FUS = focused ultrasound; MRI = magnetic resonance imaging; RF = radiofrequency.

Table 2. Clinically relevant ultrasound parameters for blood–brain barrier opening in vivo using the neuronavigation-guided focused ultrasound system

Parameter	Value
Center frequency	0.25 MHz
Derated peak-negative pressure	0.2 $\text{MPa}_{\text{pk-neg}}$
Mechanical index	0.4
Definity microbubble dose	10 µL/kg (1 × clinical dose)
Pulse length	10 ms or 2500 cycles
Pulse repetition frequency	2 Hz
Sonication duration	2 min

Microbubble acoustic emissions were recorded (sampling frequency: 50 MHz, capture length: 10 ms) with a 1.5-MHz passive cavitation detector (PCD; diameter: 32 mm, focal depth: 114 mm, ndtXducer, Northborough, MA, USA). PCD provides information on the cavitation magnitude, duration and mode within the focal volume, using either separate transducers (Tung et al. 2010) or a therapeutic transducer alone (Heymans et al. 2017). Cavitation signals also provide indirect information about the microbubble velocity through the Doppler effect, which can be captured either with a single-element PCD (Pouliopoulos and Choi 2016) or using an array of receivers (Pouliopoulos et al. 2017). Here, we used PCD to define the cavitation mode *in vitro* and *in vivo* by calculating the stable cavitation dose (SCD) and inertial cavitation dose (ICD), as described before (Tung et al. 2010). Briefly, the recorded time-domain signals were transformed into the frequency domain through a fast Fourier transform (segment size: 524,288 data points), performed in MATLAB (The MathWorks, Natick, MA, USA). Three spectral areas were filtered to derive the relevant cavitation levels or cavitation dose per pulse as follows:

1. Harmonic peaks, $f_{h,n} = nf_c$
2. Ultraharmonic peaks, $f_{u,n} = (n - 1/2)f_c$
3. Broadband emissions f_b with $f_{h,n} + 10\,\text{kHz} < f_b < f_{u,n} - 10\,\text{kHz}$ and $f_{u,n} + 10\,\text{kHz} < f_b < f_{h,n+1} - 10\,\text{kHz}$

Here, f_c is the center frequency (*i.e.,* 0.25 MHz) and n the harmonic number ($n = 3, 4, 5, \ldots, 10$). Fundamental and second harmonics were excluded from the calculations because of the strong skull reflections at these frequencies in control experiments.

Stable harmonic (dSCD_h), stable ultraharmonic (dSDC_u) and inertial cavitation (dICD) levels were then calculated as the mean root-mean-square (RMS) of the maximum absolute Fast Fourier Trransform (FFT) amplitude of the detected signal within each frequency region for each acoustic pulse as follows:

$$d\mathrm{SCD_h} = \sqrt{\left\langle \left|\mathrm{FFT}\right|_{\mathrm{f}_{\mathrm{h},n}}^{2} \right\rangle_n}$$

$$d\mathrm{SCD_u} = \sqrt{\left\langle \left|\mathrm{FFT}\right|_{\mathrm{f}_{u,n}}^{2} \right\rangle_n}$$

$$d\mathrm{ICD} = \sqrt{\left\langle \left|\mathrm{FFT}\right|_{\mathrm{f}_{b}}^{2} \right\rangle}.$$

The total cavitation dose *in vivo* was calculated as the sum of all the cavitation levels throughout the FUS treatment:

$$\mathrm{SCD_h} = \sum_{t=0}^{T} d\mathrm{SCD}_{\mathrm{h},t}$$

$$\mathrm{SCD_u} = \sum_{t=0}^{T} d\mathrm{SCD}_{\mathrm{u},t}$$

$$\mathrm{ICD} = \sum_{t=0}^{T} d\mathrm{ICD}_t$$

The total sonication duration was $T = 2$ min.

In vitro *characterization*

Skull-induced aberrations were characterized in a water tank. A capsule hydrophone (HGL-0200, ±3-dB frequency range: 0.25−40 MHz, electrode aperture: 200 µm; Onda Corp., Sunnyvale, CA, USA) was used to measure the emitted pressure profiles in free field and with a human skull fragment in the beam path. The skull fragment was submerged in water and degassed before the experiment using a vacuum pump, to reduce the gas content within the bone. Raster scans around the focal point were performed at a spatial resolution of 0.1 mm laterally and 1 mm axially. The scans had lateral/elevational and axial ranges of 10 and 60 mm, respectively, and were centered at the geometric focus of the FUS transducer (110 mm from transducer surface). Shifts along the lateral and elevational dimensions were averaged, assuming an axisymmetric distortion of the beam. Ultrasound pressure transmission coefficient through the human skull was calculated (in %) by dividing the maximum pressure of the focal volume after the skull placement by the maximum pressure of the focal volume in free field, for both simulations and experiments. Transcranial pressure loss was calculated as 100% − transmission coefficient. To determine the ultrasound attenuation through an NHP skull, we used the same setup, replacing the human skull fragment with a NHP skull fragment. The human and NHP skull fragments were positioned right on top of the water cone and at a perpendicular incidence angle, to imitate the clinical scenario. Pressure profiles and transcranial loss were expected to be extremely sensitive to the incidence angle and distance from the transducer surface. Here, we tested only one incidence angle (*i.e.,* ~90°) and transducer surface−skull distance (*i.e.,* 62 mm), which are clinically relevant for treatment of dorsolateral prefrontal cortex. Pressure profiles and losses were estimated at skull locations of variable thickness (n = 10, thickness range: 3−7.5 mm, measured with a caliper), as attenuation depends on the skull thickness (Gerstenmayer et al. 2018). All reported pressure values refer to the derated peak-negative pressure.

Cavitation detection through the human skull was also conducted within a water tank. A 0.8-mm silicon elastomer tube was submerged and fixed at a horizontal position within the focal volume of the clinical transducer (120 mm from transducer surface). The tube was filled with either water, which served as a control, or Definity microbubbles (0.2 mL microbubbles/L of solution) flowing at a rate of 1.8 mL/min. Measurements were conducted both in free field and with the human skull fragment in the beam path, positioned 62 mm away from the transducer surface. We tested three derated acoustic pressures, 200, 300 and 400 kPa, corresponding to MIs of 0.4, 0.6 and 0.8, respectively. Cavitation levels were calculated across the experimental conditions (n = 10 consecutive pulses per condition) to establish the ability of the PCD transducer to detect cavitation signals through the human skull at each acoustic pressure.

In separate experiments, a tissue-implantable type-T thermocouple (Physitemp instruments, Clifton, NJ, USA) was attached to the skull surface to measure the heating profile during clinically relevant FUS exposure (MI: 0.4−0.8, duty cycle: 2%; Table 2). A positive control sonication at a higher duty cycle (20% at an MI of 0.8) was conducted to compare with the low-duty-cycle BBB opening scheme. Temperature data were recorded at a sampling rate of 100 samples/s. Temperature increase on the skull surface was calculated by subtracting the temperature before FUS exposure from the value measured during FUS exposure (n = 3).

In vivo *feasibility*

All animal experiments were reviewed and approved by the local Institutional Animal Care and Use Committee prior to all performed studies and were in accordance with the National Institutes of Health guidelines for animal welfare. Two male adult Rhesus macaques (weight: 8−11 kg, age: 12−20 y) were treated with the clinical FUS transducer, targeting the thalamus

(NHP 1) and the dorsolateral prefrontal cortex (NHP 2), to examine the performance of the system at both cortical and subcortical regions. To accommodate the NHP experiment, the patient chair (Fig. 1) was replaced with a surgical table equipped with a stereotactic apparatus for head fixation. NHPs were initially sedated with a mixture of ketamine (10 mg/kg) and atropine (0.02 mg/kg) through intramuscular injection. Once sedated, the animals were intubated and catheterized via the saphenous vein. Anesthesia was induced and maintained throughout the experiment using inhalable isoflurane mixed with oxygen (1%−2%).

The ultrasound parameters used here (Table 2) were identical to those approved by the FDA for use in Alzheimer's patients using our system (derated peak-negative pressure: 0.2 MPa, pulse length: 10 ms, pulse repetition frequency: 2 Hz, total sonication duration: 2 min). We maintained the MI below the FDA-approved limit for ultrasound imaging applications with Definity microbubbles to avoid compromising safety. BBB opening in the NHP model was attempted at a peak-negative pressure of 0.2 MPa or an MI of 0.4. This MI is approximately five times lower than the maximum MI approved by the FDA for imaging applications (*i.e.,* MI of 1.9), twice lower than the BBB opening threshold found by Carpentier et al. (2016) in humans and similar to the threshold found in our previous NHP studies (Wu et al. 2018). In contrast to our previous studies that used 4- to 5-μm size-isolated microbubbles at a dose of 2.5×10^8 microbubbles/kg (Karakatsani et al. 2017; Wu et al. 2018), here we used commercially available Definity microbubbles at the FDA-approved clinical dose for ultrasound imaging applications (*i.e.,* 10 μL/kg). Definity microbubbles were infused as a bolus via a single injection, on treatment initiation.

Blood−brain barrier opening was assessed approximately 60 min post-sonication with T_1-weighted MRI (3-D spoiled gradient-echo, TR/TE: 20/1.4 ms, flip angle: 30°, number of excitations [NEX]: 2, spatial resolution: 500×500 μm^2, slice thickness: 1 mm with no inter-slice gap). T_1-weighted scans were acquired before and after intravenous administration of 0.2 mL/kg gadodiamide MRI contrast agent (Omniscan; GE Healthcare, Bronx, NY, USA), which is normally impermeable to the BBB (molecular weight: 591.7 Da). BBB opening was quantified by comparing pre- and post-contrast administration T_1 scans. Safety outcomes were assessed with axial T_2-weighted MRI (TR/TE: 3000/80 ms, flip angle: 90°, NEX: 3, spatial resolution: 400×400 μm^2, slice thickness: 2 mm with no inter-slice gap) and susceptibility-weighted imaging (SWI; TR/TE: 19/27 ms; flip angle: 15°, NEX: 1, spatial resolution: 400×400 μm^2; slice thickness: 1 mm with no inter-slice gap). All scans were performed in a 3-T clinical MRI scanner.

BBB opening quantification

We developed a graphics user interface (GUI) in MATLAB for BBB opening quantification and analysis. To calculate the BBB opening volume, the pre-contrast T_1 scan was subtracted from the post-contrast T_1 scan. An intensity threshold was set to isolate the BBB opening area in the difference image, and a contour plot was applied to the pixels above the threshold within the selected region of interest. The area of the BBB opening contour was calculated for each coronal MRI slice, and the total BBB opening volume (in mm^3) was found by summing the BBB opening areas in all slices.

Statistical analysis

All measurements presented here are expressed as the mean ± standard deviation. Simulations were performed for $n = 4$ pulse lengths and $n = 6$ transducer axial positions. Cavitation detection was established by comparing control and microbubble-seeded cavitation levels in free field and through the human skull, using a two-sample *t*-test in MATLAB ($n = 10$ pulses). Statistically significant differences were assumed at $p < 0.05$.

RESULTS

Numerical simulations

Numerical simulations revealed that transducer 3 was able to target the brain median plane while maintaining a tightly focused beam, without multiple sidelobes (Fig. 2). Transducer 1 did not have sufficient radius of curvature to produce a long enough focal depth for the human skull, because of its low *f*-number. Transducer 2 produced multiple sidelobes similar in amplitude to the main lobe because of the large *f*-number and the low outer-to-inner diameter ratio. Furthermore, the focal volume was subject to greater distortion because of the higher center frequency compared with transducers 1 and 3 (0.35 MHz vs. 0.2 MHz and 0.25 MHz). We found that in the case of a single-element transducer, an *f*-number of 1 (transducer 3) was more suitable for applications in the human brain, compared with lower or larger *f*-numbers within the subset we have tested.

Such a transducer design allows targeting of both superficial cortical areas and deeper subcortical areas (Fig. 3). By physically moving the FUS transducer toward/away from the skull surface, one can achieve a treatment envelope up to 80 mm in depth. Simulations revealed that the focal dimensions, pressure profile and skull-induced focal shift depend on the transducer axial offset and the pulse length (Fig. 4). The transducer axial offset was defined as the distance of the free-field focus from the simulation center ($x = 0$ mm). Intracranial acoustic pressures only moderately changed throughout the axial offsets. Highest pressures were observed near

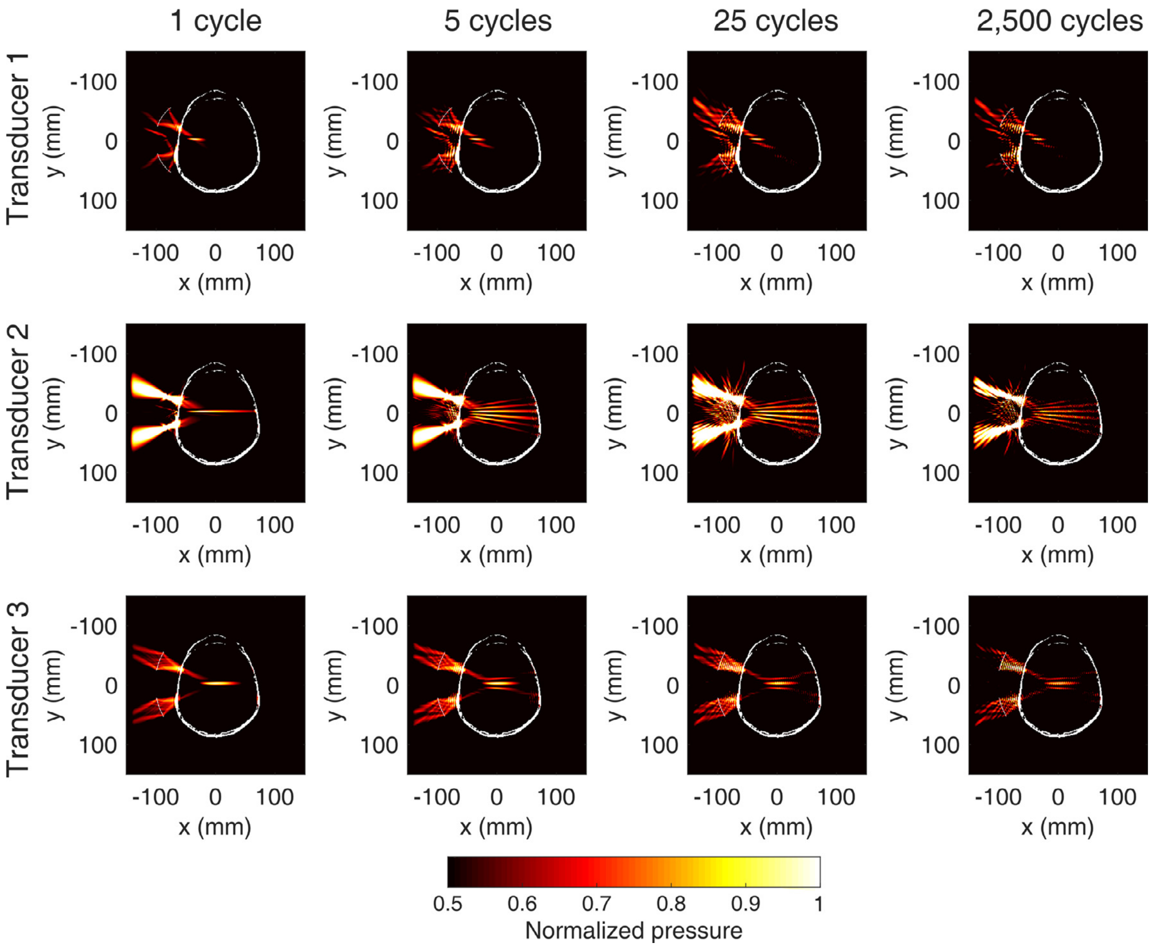

Fig. 2. Numerical simulations of ultrasound propagation with different single-element transducers (top to bottom: 1, 2, 3) emitting pulses of variable length (left to right: 1, 5, 25, 2500 cycles). Transducer 3 was the only configuration that was able to treat deep structures without presenting multiple sidelobes within the human skull. Color bar: Normalized focal pressure. Each pressure profile was self-normalized to the maximum acoustic pressure within the skull to illustrate the −3-dB focal volume. Pressure values refer to the maximum instantaneous pressure at each location.

the skull center, while there was a decrease of up to 7% toward the proximal and distal skull. The amplitude of lateral sidelobes increased with pulse length, from 49% of the main lobe at 1 cycle to 76% of the main lobe at 2500 cycles. All pressure profiles shown in Figures 2 and 3 were normalized to the maximum pressure within the skull and plotted in the range [0.5, 1], to visualize the −3-dB focal volume following transcranial ultrasound propagation.

Pulse lengths longer than 1 cycle produced constructive and destructive interference at the distal part of skull, with nodes and antinodes appearing at a spacing of half-wavelength (*i.e.,* 3 mm). The interference spatial extent was equal to half the spatial length of the acoustic pulse (*e.g.,* 2.5 cycles or 15 mm for a pulse length of 5 cycles or 30 mm). For the clinically relevant pulse length of 2500 cycles, the interference profile reached equilibrium and extended throughout the interior of the human skull. The theoretical limit for standing wave generation at 0.25 MHz and a skull size of 130 mm is 43 cycles.

The presence of the human skull led to the distortion and spatial shift of the simulated focal volume (Fig. 5). In water medium without the human skull, the axial and lateral full widths at half-maximum (FWHM) were simulated to be 65.5 × 5.6 mm. The focal width and length were reduced by 2.7 ± 2.4% and by 8.4 ± 4.8% along the lateral and axial dimensions, respectively, because of skull-induced aberrations ($n = 4$ pulse lengths and $n = 6$ transducer positions). The focus was also negatively shifted toward the transducer (Fig. 5b). Axial shifts depended on the transducer position. Interestingly, shifts were smaller for larger offsets. In other words, the farther the focus from the brain midline, the smaller the axial shift. On average, the axial and lateral focal shifts were 6.1 ± 2.4 and 0.1 ± 0.2 mm, respectively (Fig. 5c). Pressure attenuation caused by the

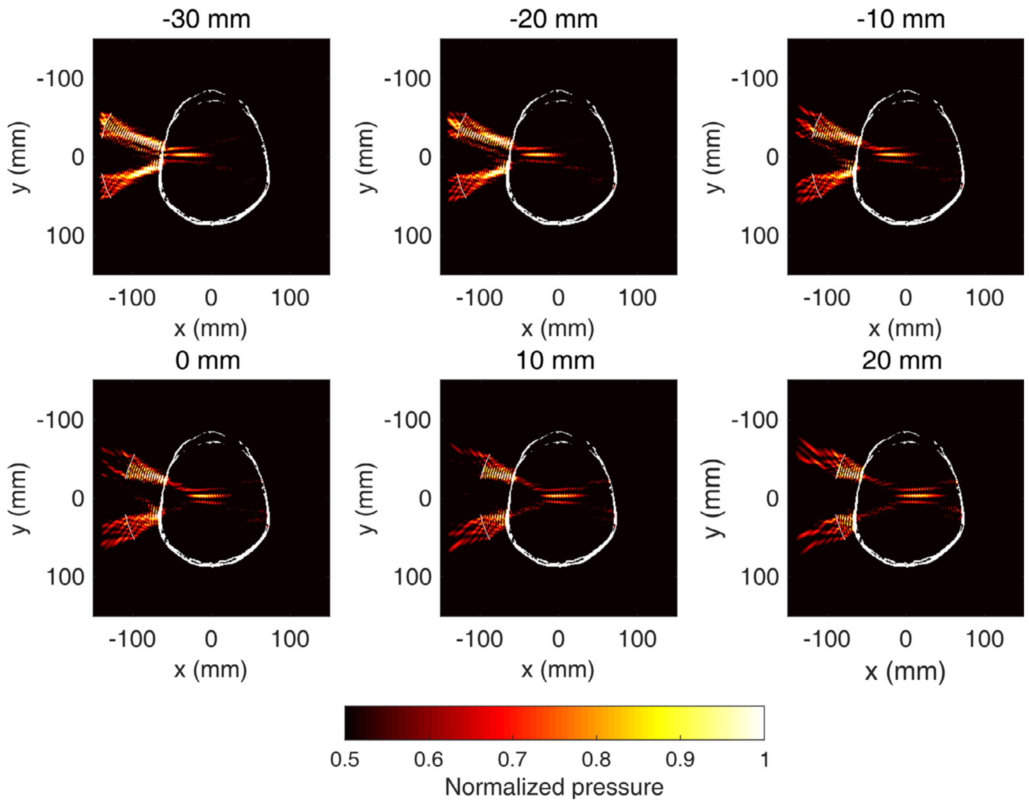

Fig. 3. Numerical simulations of ultrasound propagation with the clinical focused ultrasound transducer targeting structures of variable depth within a human skull. Examples are shown for transducer axial offset of −30 to 20 mm (offset = 0 mm when the focus in free-field coincides with the midline). Center frequency: 0.25 MHz, pulse length: 2500 cycles. Color bar: normalized focal pressure. Each pressure profile was self-normalized to the maximum acoustic pressure within the skull to illustrate the −3-dB focal volume. Pressure values refer to the maximum instantaneous pressure at each location.

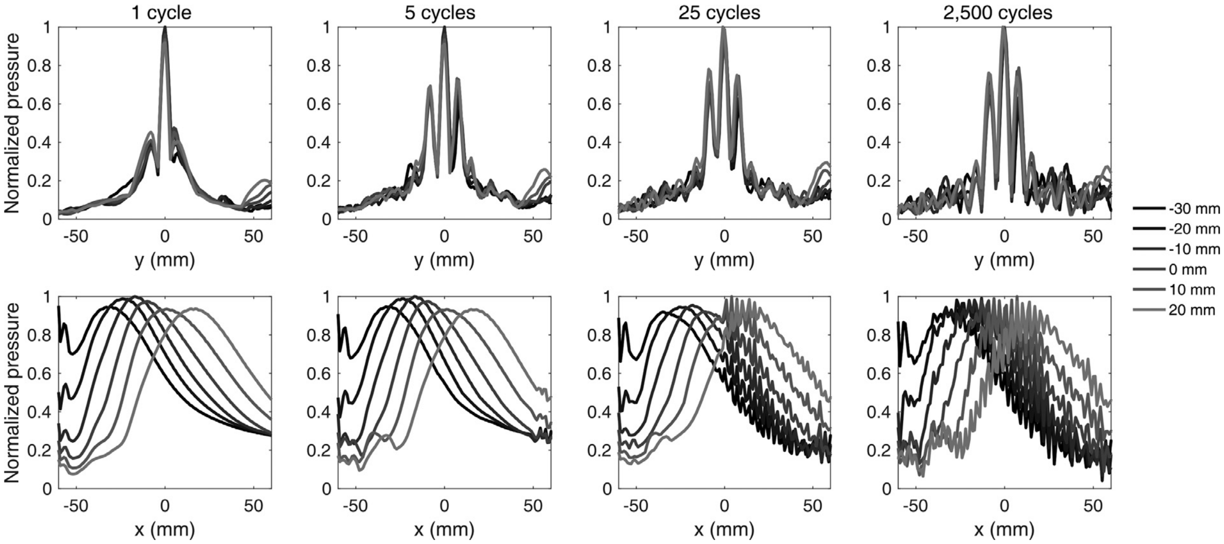

Fig. 4. Lateral (top) and axial (bottom) profiles of the simulated pressure field within a human skull. Lateral sidelobes and interference patterns emerge for pulse lengths larger than one cycle. The spatial length of interference away from the distal skull bone increases linearly with the pulse length.

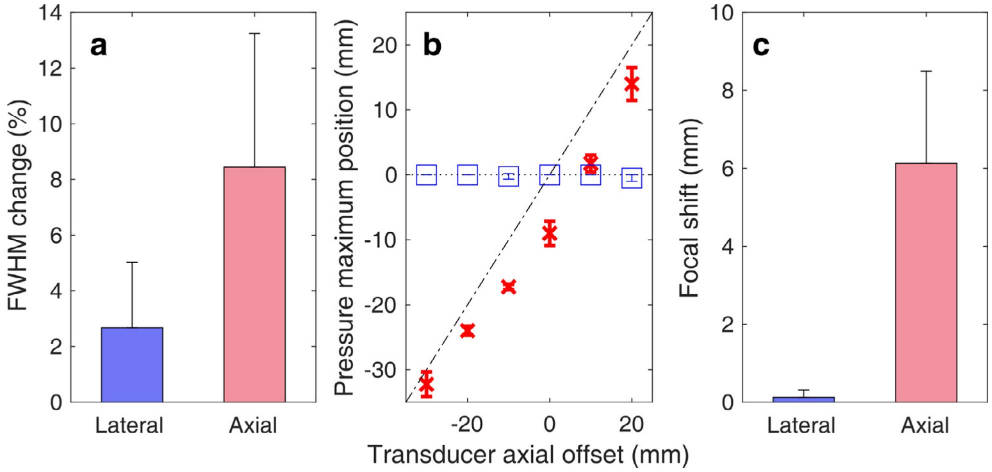

Fig. 5. Simulated human skull-induced focal distortion. (a) Full width at half maximum (FHWM) change caused by the presence of the human skull. FWHM changes were first averaged across the pulse lengths for each axial offset (n = 4 pulse lengths), and then averaged across all depths (n = 6 axial offsets). (b) Simulated focal shifts along the axial (red crosses) and lateral (blue boxes) dimensions. Diagonal dotted-dashed line and parallel dotted line denote axial and lateral shifts equal to zero, respectively (n = 4 pulse lengths). (c) Average focal shifts across the lateral and axial dimensions (n = 6 axial offsets). Data are expressed as the mean ± standard deviation.

human skull was simulated to be 36.1 ± 3.4% (n = 10 different CT slices).

In vitro *characterization*

To confirm the simulation findings, we performed a detailed estimation of the 2-D beam profiles along the lateral/elevational and lateral/axial dimensions, with and without the presence of a human skull fragment (Fig. 6). Using the capsule hydrophone and the 3-D positioning system (Fig. 6a), we measured the pressure profiles along the axial, lateral and elevational dimensions. The free-field focal length and width were 47.6 × 5.6 mm (Fig. 6b, 6c: left side). These values were close to the nominal focal dimensions of 49 × 6 mm provided by the manufacturer. Ultrasound propagation through the human skull was expected to attenuate and shift the acoustic focus. Inserting the skull fragment within the beam path attenuated the pressure amplitude by 44.4 ± 1.3% and distorted the focal region (Fig. 6b, 6c: right side). The lateral and axial FWHMs decreased by 3.3 ± 1.5% and 3.9 ± 1.8%, respectively (Fig. 6d). Experimental focal shifts along the lateral and axial dimensions were 0.5 ± 0.4 and 2.1 ± 1.1 mm, respectively (Fig. 6e).

Passive cavitation detection measurements confirmed that the 1.5-MHz PCD transducer can detect cavitation signals through the human skull (Fig. 7). Using the *in vitro* setup described earlier (Fig. 7a), we detected stationary reflections at the fundamental and the second harmonic for the control experiment, both from the tube and from the human skull (Fig. 7b). When Definity microbubbles were flowing through the vessel phantom, we observed a rise in the higher harmonics (up to the fifth harmonic or 1.25 MHz) and ultraharmonics (up to the third ultraharmonic or 0.825 MHz).

Higher acoustic pressures led in general to higher harmonic and ultraharmonic peaks. In Figure 7d, light-color bars represent control sonications, while dark-color bars represent sonications with Definity microbubbles. The two leftmost bars in each cavitation dose represent free-field sonications, while the two rightmost bars represent sonications through the human skull fragment. Ten distinct therapeutic pulses were emitted for each condition. Harmonic stable cavitation levels were significantly higher for microbubbles than the control, for MIs of 0.4 and 0.6 both in free-field and through the human skull (Fig. 7d). Ultraharmonic stable cavitation levels with microbubbles were significantly higher than those of the control at MIs of 0.4 and 0.6 only in free-field. There was a significant difference through the human skull at an MI of 0.4, but a non-significant increase at an MI of 0.6. At the highest acoustic pressure, stable harmonic and inertial cavitation levels were significantly higher for the control than for microbubbles. This was likely due to inadequate degassing of the human skull fragment, which resulted in intracranial cavitation nuclei in the control experiment. Inertial cavitation levels rose considerably above the noise level at all MIs in free-field, and also during the control experiments in the presence of skull for MIs of 0.6 and 0.8.

Next, we measured the ultrasound-induced heating during clinically relevant ultrasound exposure. A wire thermocouple was attached below the human skull fragment and within the ultrasound beam path. To simulate the clinical scenario, 2-min sonications were performed

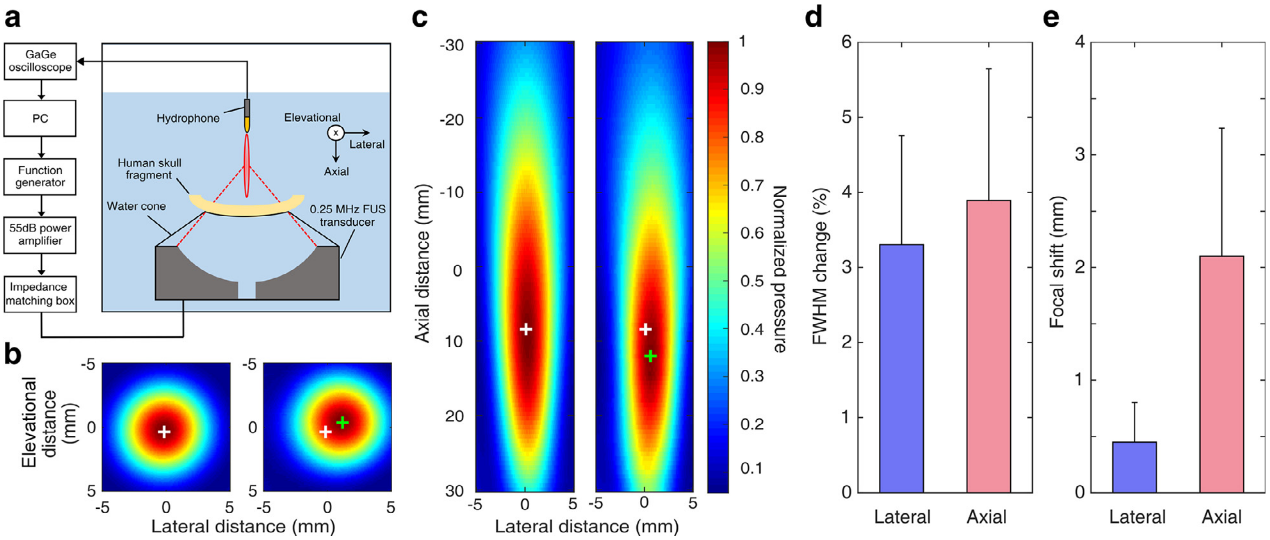

Fig. 6. Experimental human skull-induced focal distortion. (a) Experimental setup for measuring focal distortion using a hydrophone. A raster scan was performed to measure the focal volume in (b, c—left side) free field and (b, c—right side) with a human skull fragment. Pressure maximum was 10 mm closer to the transducer compared with the geometric focus. White crosses denote the position of the free-field focus. Green crosses denote the position of the focus following transcranial propagation. (d) Full width at half maximum change and (e) focal shifts along the lateral and axial dimensions. Data are expressed as the mean ± standard deviation (n = 10 scans with ultrasound propagating through skull segments of different thickness). FUS = focused ultrasound; FWHM = full width at half-maximum.

using the parameters intended for the clinic (Table 2). The maximum temperature increase was between 0.11 ± 0.05˚C and 0.16 ± 0.03˚C (n = 3) during sonication at MIs of 0.4—0.8 (Fig. 8). This negligible heating was expected, given the low duty cycle of ultrasonic pulse sequences used in BBB opening (*i.e.,* 2%). A control sonication at 10 × higher duty cycle (*i.e.,* 20%) and an MI of 0.8 did increase the temperature by 0.59 ± 0.23˚C.

In vivo *feasibility*

Finally, we tested the proposed clinical system in an NHP model to perform non-invasive and targeted BBB opening at a peak-negative pressure of 200 kPa or an MI of 0.4, using the clinically recommended Definity dose (10 µL/kg). Two NHPs were treated targeting the thalamus (NHP 1) and the dorsolateral prefrontal cortex (NHP 2). The two targets were selected as examples of deep and superficial structures, respectively. Despite the low pressure and microbubble dose, we achieved BBB opening in both targeted structures (Fig. 9). BBB opening was more pronounced in the gray matter rather than in the white matter tracts, as reported before (Karakatsani et al. 2017). The total BBB opening volume was 153 mm^3 for NHP 1 and 164 mm^3 for NHP 2. Safety was evaluated with T_2-weighted MRI and SWI (Fig. 9). There was neither a hyper-intense region in T_2 scans nor a hypo-intense region in SWI an hour post-sonication, indicating lack of hemorrhage or edema in the sonicated region. Although this was an acute safety evaluation, we did not expect any long-term effects at this low-pressure regime, based on our previous studies (Downs et al. 2015).

Safety outcomes were corroborated by the captured PCD data which confirmed in real time the absence of violent cavitation events within the focal volume (Fig. 10). Before microbubble administration, the spectral content of the received signals included the fundamental frequency (*i.e.,* 0.25 MHz) and the first two or three harmonics (Fig. 10a, 10d). Following microbubble bolus injection, there was an increase in higher harmonics and, for NHP 2, ultraharmonics (Fig. 10b, 10e). However, there was no considerable increase in the broadband signal floor following microbubble administration (*white dashed line*), as illustrated in the spectrograms of both FUS treatments (Fig. 10c, 10f). These qualitative traits were quantified with SCD and ICD (Fig. 10g—i). SCD_h increased by 5.44 ± 1.16-fold on microbubble infusion ($t > 15$ s), while SCD_u and ICD increased by 1.46 ± 0.01- and 1.48 ± 0.21-fold, respectively. We can thus infer that microbubbles underwent stable and recurrent oscillations, with stable cavitation dominating over transient and inertial cavitation throughout treatment. On average, the total cavitation dose was $1.37 \pm 0.17 \times 10^4$ mV.

DISCUSSION

A clinical system using a single-element transducer and neuronavigation guidance for BBB opening offers distinct advantages compared with alternative approaches. First, BBB opening can be achieved in a

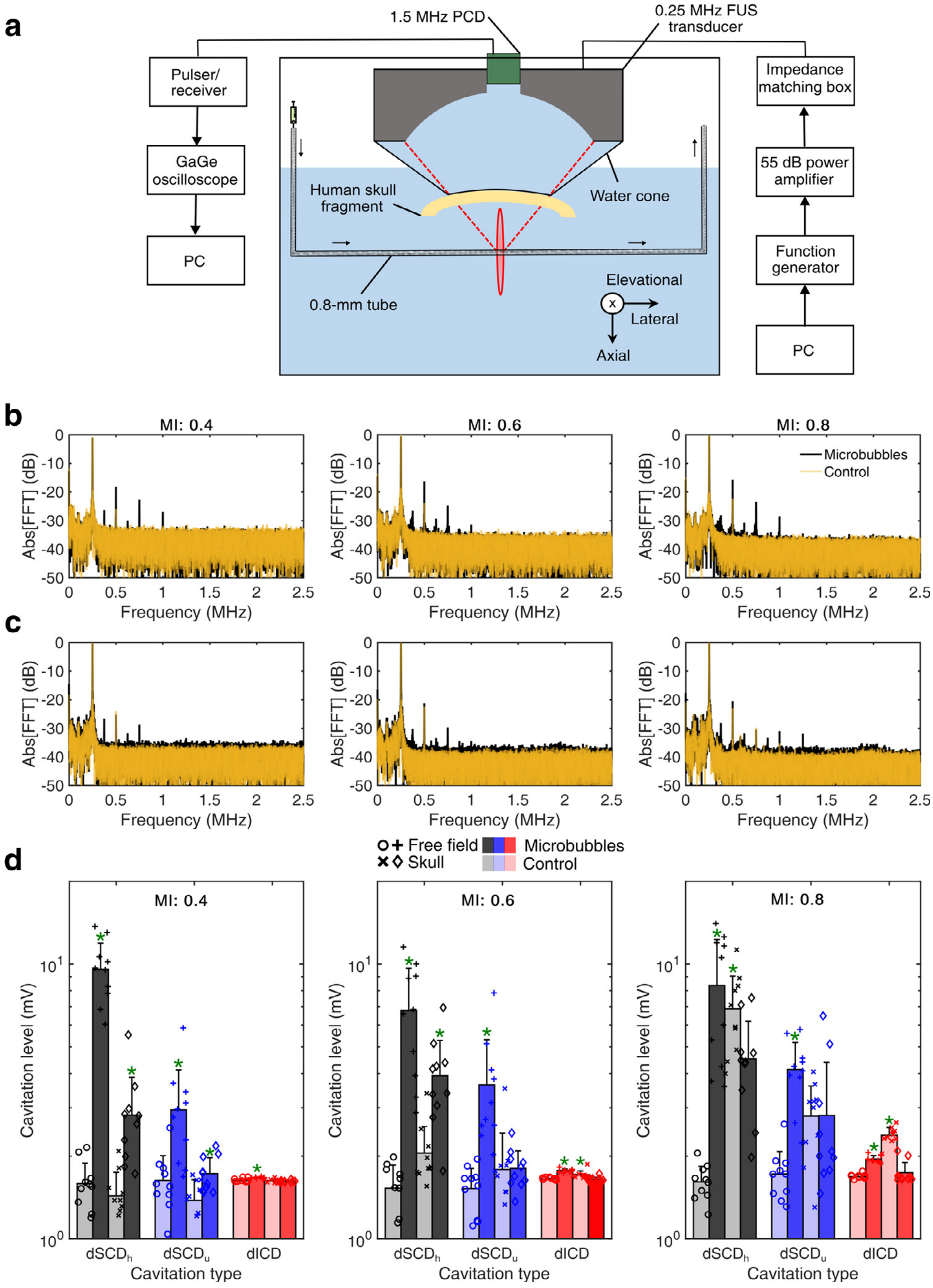

Fig. 7. Passive cavitation detection through the human skull. (a) In vitro setup for passive cavitation detection. A 0.8-mm tube filled with Definity microbubbles was used as a vessel-mimicking phantom. (b) Spectra of control (transparent orange line) and microbubble (black line) acoustic emissions for mechanical indexes (MIs) of 0.4 (left), 0.6 (middle) and 0.8 (right) in free-field. (c) Spectra of control and microbubble acoustic emissions through the human skull. (d) Cavitation levels in free-field (circles, plus signs) and through the human skull (crosses, diamonds), for control (light bars) and microbubbles (dark bars), at MIs of 0.4 (left), 0.6 (middle) and 0.8 (right). Data are expressed as the mean ± standard deviation (n = 10 pulses). *$p < 0.05$. FFT = fast Fourier transform; FUS = focused ultrasound; PCD = passive cavitation detector.

non-invasive manner, which is preferable especially for long-term repeated treatments required in AD or PD. Second, such a system can provide access to both shallow (*i.e.,* cortical) and deep (*i.e.,* subcortical) brain regions (Figs. 3–5), although at the expense of a large axial-to-lateral focal size ratio and variable focal distortion in different depths (Fig. 5). Also, there is no need for an MRI system during BBB opening which may be a

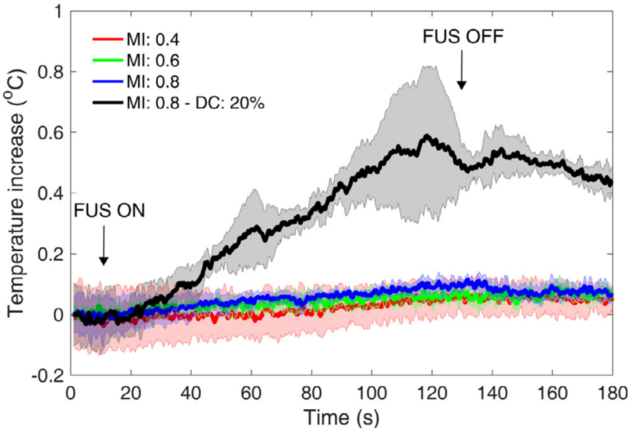

Fig. 8. Skull heating using the clinical focused ultrasound transducer at mechanical indexes (MIs) of 0.4 (red line), 0.6 (green line) and 0.8 (blue line) and clinically relevant ultrasound parameters (center frequency: 0.25 MHz, pulse length: 2500 cycles or 10 ms, pulse repetition frequency: 2 Hz, duty cycle: 2%, total duration: 2 min). A higher duty cycle (i.e., DC: 20%) was used as a positive control for heating (black line). Data are expressed as the mean ± standard deviation (n = 3).

costly and formidable hurdle for widespread use of FUS-mediated treatments, especially given that temperature elevation is not incurred. Neuronavigation systems are typically available for neurosurgical procedures (Grunert et al. 2003), so the additional cost for hospitals is the single-element transducer, the driving electronics and the robotic arm. The targeting and sonication procedure is efficient and simple (<30 min) as opposed to MR-guided FUS treatment (3−4 h). Moreover, the NgFUS is portable so treatment can take place at any location without the need of an MRI unit. Finally, low-frequency and low-duty-cycle treatment leads to limited skull-induced aberrations (Figs. 5 and 6) and FUS-induced skull heating (Fig. 8), respectively.

Lower frequencies favor cavitation-mediated bioeffects at low acoustic pressures (Apfel and Holland 1991; Ilovitsh et al. 2018). We have shown here that the BBB can be opened in an NHP model at an MI of 0.4 (Fig. 9), which is twice lower than the minimum MI required using the unfocused implanted 1.05-MHz transducer in humans (Carpentier et al. 2016) and similar to other NHP studies (McDannold et al. 2012; Downs et al. 2015; Karakatsani et al. 2017; Wu et al. 2018). Low-pressure treatments not only ensure safety (Fig. 9), but also facilitate regulatory approval because they are compatible with routinely used ultrasound imaging protocols. Such acoustic pressure instigates cavitation activity that is detectable in real time with the co-aligned PCD transducer (Fig. 7), with stable cavitation emissions dominating the spectra during FUS treatment in an NHP model (Fig. 10). Clinically relevant parameters (Table 2) are thus not expected to lead to violent inertial cavitation, which was detected in higher-MI sonication (Fig. 7).

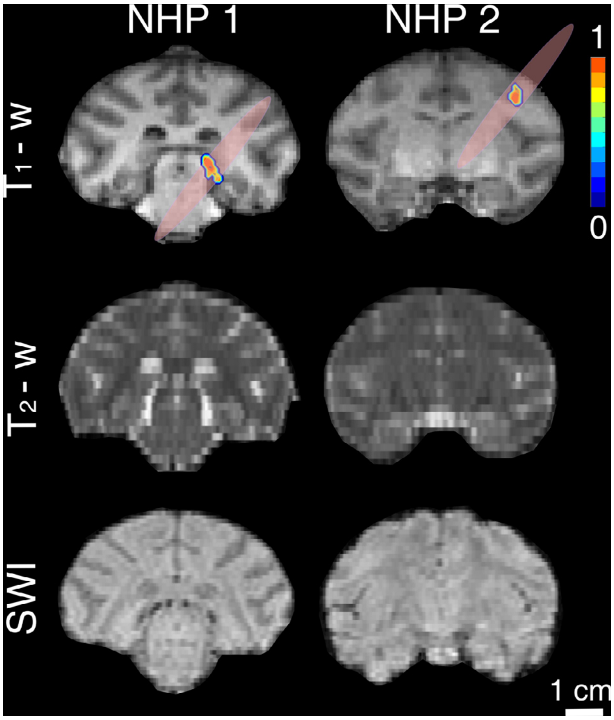

Fig. 9. In vivo feasibility in a non-human primate (NHP) model. Coronal T_1-weighted, T_2-weighted and susceptibility-weighted imaging (SWI) for NHPs 1 (left) and 2 (right). T_1-Weighted magnetic resonance imaging-confirmed blood−brain barrier opening in the thalamus (NHP 1) and dorsolateral prefrontal cortex (NHP 2), using the clinical focused ultrasound (FUS) transducer with clinically relevant parameters (MI: 0.4) and U.S. Food and Drug Administration-approved Definity microbubble dose (10 µL/kg). T_2-Weighted imaging and SWI revealed that there is no acute hemorrhage or edema after the FUS treatment. Color bar: Normalized contrast enhancement. Bar = 1 cm.

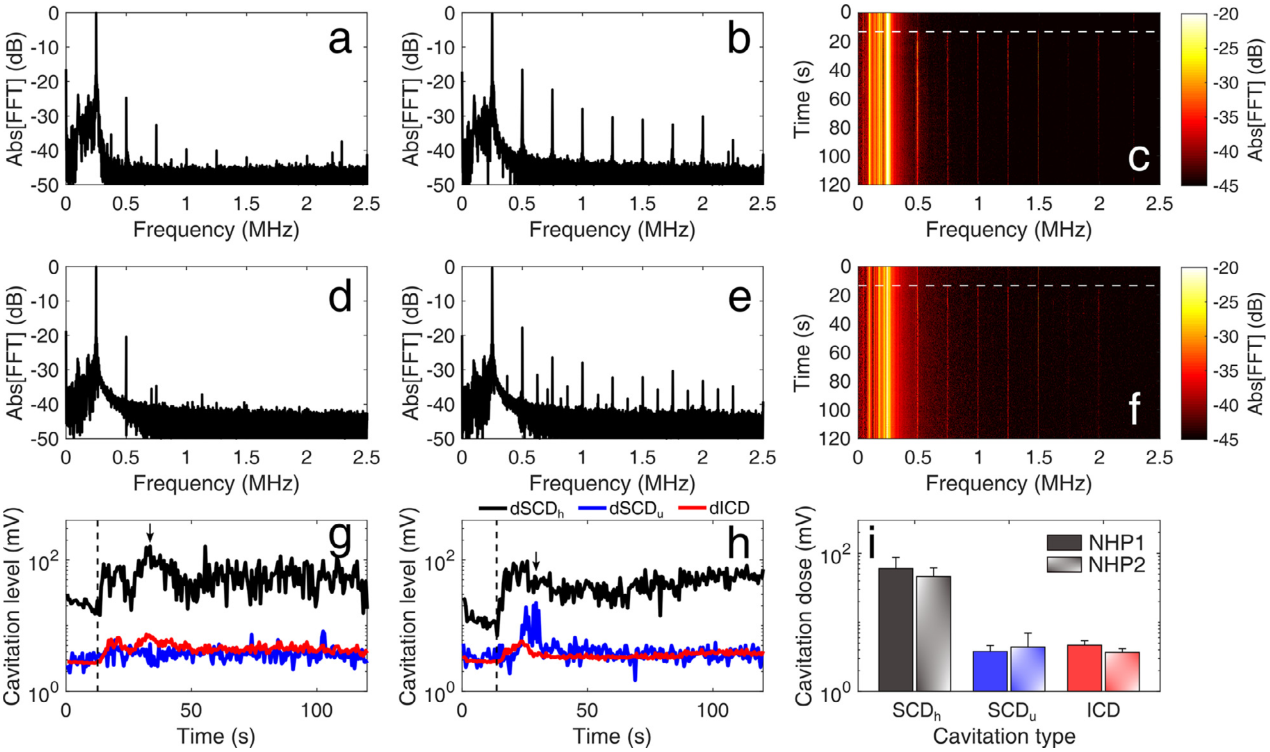

Fig. 10. In vivo passive cavitation detection measurements confirmed that stable cavitation dominated throughout ultrasound treatment at clinically relevant conditions. Spectral amplitude (a, d) before and (b, e) after microbubble injection, for non-human primate (NHP) 1 (a, b) and NHP 2 (d, e). Spectrogram of the entire treatment session for NHP 1 (c) and NHP 2 (f). Higher harmonic emissions were detected, with no substantial increase in the broadband floor after microbubble entrance into the focal volume (white dashed lines). (g, h) Stable harmonic cavitation levels (black line) rose right after microbubble administration (dashed line) and remained relatively constant throughout the sonication, for both NHP 1 (g) and NHP 2 (h). Stable ultraharmonic (blue line) and inertial cavitation levels (red line) had a moderate increase, indicating absence of violent cavitation events at an MI of 0.4. Arrows indicate the time points shown in (b) and (e). (i) Average stable harmonic (black), stable ultraharmonic (blue) and inertial (red) cavitation dose during focused ultrasound treatment for NHP 1 (filled bars) and NHP 2 (patterned bars), following microbubble administration ($t > 15$ s). Data are expressed as the mean ± standard deviation ($n = 210$ pulses). FFT = fast Fourier transform.

Here, we reported successful BBB opening using 10-ms-long pulses. However, such pulse lengths produce interference and standing waves within the human skull (O'Reilly et al. 2010), as illustrated here (Figs. 2−4), and promote primary (Dayton et al. 2002; Koruk et al. 2015) and secondary (Dayton et al. 1997; Lazarus et al. 2017) acoustic radiation forces, which may indirectly compromise safety. In our future work, we aim to use either coded excitation (Kamimura et al. 2015) or shorter pulses on the order of microseconds (<50 cycles) to avoid standing wave formation (O'Reilly et al. 2011). Such pulses have been reported to produce more uniform cavitation activity within the focal area by extending the microbubble lifetime (Pouliopoulos et al. 2014), avoiding cluster formation and spreading the microbubble activity in space and time (Pouliopoulos et al. 2016; Pouliopoulos 2017). *In vivo*, rapid short-pulse sequences produce uniform BBB openings that last less than 10 min and do not allow extravasation of inflammation-inducing proteins, such as albumin, into the brain parenchyma (Morse et al. 2019). On the other hand, it is more difficult to deliver large therapeutic molecules using short pulses (Choi et al. 2011).

Short pulses also allow for improved passive mapping of cavitation signals, through the synchronization of the therapeutic and imaging processes (*i.e.,* using absolute time-of-flight information) (Gateau et al. 2011; Burgess et al. 2018). PAM in either the time (Gyöngy and Coussios 2010; Coviello et al. 2015) or frequency (Salgaonkar et al. 2009; Haworth et al. 2012; Arvanitis et al. 2015a, 2017; Haworth et al. 2017; Wu et al. 2018; Burgess et al. 2018) domain can be achieved by replacing the single-element PCD transducer with a multi-element linear array operating in receive mode. Using a PAM array, one can account for skull-induced aberrations in receive and localize acoustic cavitation activity in a more precise manner (Jones et al. 2013, 2015; O'Reilly et al. 2014; Arvanitis et al. 2015b). Furthermore, we plan to use pulse inversion in the short therapeutic pulses, to be able to detect weak cavitation emissions through the thick human skull (Pouliopoulos et al. 2018). Future efforts will finally focus on using short pulses and PAM in closed-loop (Sun et al. 2017; Jones et al. 2018; Kamimura et al. 2018; Patel et al. 2019) to improve the spatiotemporal control of acoustic cavitation activity within the brain.

The proposed system is limited by a number of factors. First, the axial focal length is eight times larger than the lateral focal width. The elongated focus was necessary to increase the targetable brain coverage or treatment envelope; however, this comes at the expense of potentially asymmetric BBB opening. Hemispherical arrays provide lower axial-to-lateral focal beam width even at large steering angles, in both emission and reception modes. Second, real-time single-element PCD monitoring does not allow for either subfocal volume localization of cavitation activity or detection of cavitation signals over a large bandwidth. The clinical transducer was designed with an inner diameter of 44 mm to allow for insertion of not only single-element transducers but also multi-element arrays for passive mapping of cavitation activity. Third, the proposed system is currently capable of compensating for skull-induced aberrations by predicing, and accounting for, the shift using a simulation framework similar to the one presented herein but not by phasing the elements in a way similar to multi-element hemispherical arrays. Another possible solution is to use 3-D printed holographic phase plates tailored to each skull contour and targeted structure (Melde et al. 2016; Ferri et al. 2018; Maimbourg et al. 2018). Accurate knowledge of the intracranial pressure is impossible; therefore, one needs to simulate the pressure field within the targeted location on a patient-by-patient basis using head CT scans. However, this remains an approximation, and emitted pressures should remain below the safety limits assuming the lowest attenuation coefficient possible. Finally, the robotic system used to hold and position the transducer in place for treatment has only 4 degrees of freedom, which limits the achievable range of incidence angles. Subsequent improvements will include a robotic arm with 6 degrees of freedom.

In this study, numerical simulations were performed in 2-D space, assuming axisymmetric beam profiles along the axial dimension. However, the human skull is asymmetric and highly inhomogeneous in 3-D space; therefore the simulated profiles are a first-order approximation. The single-element transducer was simulated in k-Wave as a collection of 1-mm point sources firing simultaneously. This may be the cause of the overestimation of the axial beam width in the simulations compared with the experiment (65.53 mm vs. 47.57 mm in free field). Also, we used a human skull fragment for our experiments as opposed to a complete human skull. In previous studies from our group, we investigated the effect of varying incidence angles at the BBB opening volume (Karakatsani et al. 2017; Wu et al. 2018). Here, our primary interest was to study the effects of focusing the therapeutic beam at different depths (Figs. 3−5); thus, only one incidence angle (approximately 90^{o}) was set for both simulations and experiments. For this reason, the lateral position of the FUS transducer remained constant in the numerical simulations. Yet, there was a discrepancy between the simulated and experimental pressure losses following transcranial propagation (36% vs. 44.4%), which can be reduced by using 3-D simulations, finer grids and time steps and identical skull shapes/dimensions. In upcoming clinical trials, 3-D simulations will be performed for each patient, using a grid with isotropic resolution of 0.5 mm, a specific beam trajectory and a well-defined target within the prefrontal cortex.

On average, axial shifts were of similar magnitude to those predicted in simulations than in the experiments (Figs. 5 and 6). Averaging in the simulations was conducted over different pulse lengths and focusing depths (Fig. 5), whereas experimental measurements (Fig. 6) were conducted with a single pulse length (*i.e.,* 25 cycles) and fixed transducer−skull distance (*i.e.,* 62 mm). The axial shift in the simulation which resembled the experimental skull−transducer distance (*i.e.,* axial offset of −30 mm) was 2.25 ± 1.92 mm (Fig. 5), similar to the experimentally derived shift of 2.1 ± 1.1 mm (Fig. 6). The *in vitro* cavitation detection experiment was conducted using a single 0.8-mm vessel-mimicking tube, which does not capture the complexity and variability of the *in vivo* vasculature. Finally, although all simulations and bench-top experiments focused on the human skull, the initial *in vivo* feasibility testing of the NgFUS system was conducted using two NHPs. Although this model is the closest resemblance to humans, the safety and performance of this approach remains to be tested in the clinic.

CONCLUSIONS

We developed a clinical setup for BBB opening based on a single-element transducer with neuronavigation guidance and real-time cavitation monitoring. Using this system, one can achieve non-invasive and targeted BBB opening with limited focal distortion and induced skull heating. Lateral and axial shifts were experimentally measured to be 0.5 ± 0.4 and 2.1 ± 1.1 mm, and were simulated as 0.1 ± 0.2 and 6.1 ± 2.4 mm. We found that the focal volume decreased by 3.3 ± 1.4% and 3.9 ± 1.8% along the lateral and axial dimensions, respectively, following transmission through a human skull fragment. Maximum temperature increase on the skull surface was 0.16 ± 0.03°C. Using this clinical system, we produced a 153 ± 5.5 mm^3 BBB opening in an NHP model with clinically relevant parameters and without any detectable damage. Ongoing work is focused on the short- and long-term safety profile of the current clinical system, including histopathology and behavioral studies in multiple NHPs, and progressing onto human applications. In our future work, we plan to use the NgFUS system, which was recently granted an investigational device exemption (IDE G180140) by the FDA, to achieve non-invasive and targeted BBB opening in AD patients.

Acknowledgments—This work was supported by National Institutes of Health Grants 5R01EB009041 and 5R01AG038961. The authors acknowledge the members of the Ultrasound Elasticity and Imaging Laboratory (UEIL) at Columbia University for their contribution in the development this system. ANP thanks Javier Cudeiro for advice on the numerical simulations, Cindy Han for guidance on regulatory issues and Rogue Research Inc. for assistance with the BrainSight platform.

Conflict of interest disclosure—EEK and HASK are inventors and own intellectual property on some aspects of the technology presented herein. All other authors have no conflict of interest.

REFERENCES

Apfel RE, Holland CK. Gauging the likelihood of cavitation from short-pulse, low-duty cycle diagnostic ultrasound. Ultrasound Med Biol 1991;17:179–185.

Arvanitis CD, Livingstone MS, Vykhodtseva N, McDannold N. Controlled ultrasound-induced blood−brain barrier disruption using passive acoustic emissions monitoring. PLoS One 2012;7:e45783.

Arvanitis C, McDannold N, Clement G. Fast passive cavitation mapping with angular spectrum approach. J Acoust Soc Am 2015;138 1845−1845.

Arvanitis CD, Clement G, McDannold N. Transcranial assessment and visualization of acoustic cavitation: Modeling and experimental validation. IEEE Trans Med Imaging 2015;34:1270–1281.

Arvanitis CD, Crake C, McDannold N, Clement GT. Passive Acoustic Mapping with the Angular Spectrum Method. IEEE Trans Med Imaging 2017;36:983–993.

Arvanitis CD, Askoxylakis V, Guo Y, Datta M, Kloepper J, Ferraro GB, Bernabeu MO, Fukumura D, McDannold N, Jain RK. Mechanisms of enhanced drug delivery in brain metastases with focused ultrasound-induced blood−tumor barrier disruption. Proc Natl Acad Sci USA 2018;115 201807105.

Asquier N, Bouchoux G, Canney M, Martin C, Law-Ye B, Leclercq D, Chapelon JY, Lafon C, Idbaih A, Carpentier A. Blood−brain barrier disruption in humans using an implantable ultrasound device: Quantification with MR images and correlation with local acoustic pressure [Epub ahead of print.]. J Neurosurg 2019. doi: 10.3171/2018.9.JNS182001.

Aubry JF, Tanter M, Pernot M, Thomas JL, Fink M. Experimental demonstration of noninvasive transskull adaptive focusing based on prior computed tomography scans. J Acoust Soc Am 2003;113:84–93.

Burgess MT, Apostolakis I, Konofagou EE. Power cavitation-guided blood−brain barrier opening with focused ultrasound. Phys Med Biol 2018;63 065009.

Cancer Imaging Archive. Head−neck cetuximab. Available at: https://wiki.cancerimagingarchive.net/display/Public/Head-Neck+Cetuximab. 2017.

Carpentier A, Canney M, Vignot A, Reina V, Beccaria K, Horodyckid C, Karachi C, Leclercq D, Lafon C, Chapelon JY, Capelle L, Cornu P, Sanson M, Hoang-Xuan K, Delattre JY, Idbaih A. Clinical trial of blood−brain barrier disruption by pulsed ultrasound. Sci Transl Med 2016;8(343) LP-343re2.

Choi JJ, Pernot M, Small SA, Konofagou EE. Noninvasive, transcranial and localized opening of the blood−brain barrier using focused ultrasound in mice. Ultrasound Med Biol 2007;33:95–104.

Choi JJ, Selert K, Vlachos F, Wong A, Konofagou EE. Noninvasive and localized neuronal delivery using short ultrasonic pulses and microbubbles. Proc Natl Acad Sci USA 2011;108:16539–16544.

Clement GT, Hynynen K. A non-invasive method for focusing ultrasound through the human skull. Phys Med Biol 2002;47:1219.

Cosgrove D, Harvey C. Clinical uses of microbubbles in diagnosis and treatment. Med Biol Eng Comput 2009;47:813–826.

Coussios CC, Roy RA. Applications of acoustics and cavitation to noninvasive therapy and drug delivery. Annu Rev Fluid Mech 2008;40:395–420.

Coviello C, Kozick R, Choi J, Gyöngy M, Jensen C, Smith PP, Coussios CC. Passive acoustic mapping utilizing optimal beamforming in ultrasound therapy monitoring. J Acoust Soc Am 2015;137:2573.

Dayton P, Morgan K, Klibanov A, Brandenburger G, Nightingale K, Ferrara K. A preliminary evaluation of the effects of primary and secondary radiation forces on acoustic contrast agents. IEEE Trans Ultrason Ferroelectr Freq Control 1997;44:1264–1277.

Dayton PA, Allen JS, Ferrara KW. The magnitude of radiation force on ultrasound contrast agents. J Acoust Soc Am 2002;112:2183–2192.

Downs ME, Buch A, Sierra C, Karakatsani ME, Chen S, Konofagou EE, Ferrera VP. Long-term safety of repeated blood−brain barrier opening via focused ultrasound with microbubbles in non-human primates performing a cognitive task. PLoS One 2015;10 e0125911.

Elias WJ, Lipsman N, Ondo WG, Ghanouni P, Kim YG, Lee W, Schwartz M, Hynynen K, Lozano AM, Shah BB, Huss D, Dallapiazza RF, Gwinn R, Witt J, Ro S, Eisenberg HM, Fishman PS, Gandhi D, Halpern CH, Chuang R, Butts Pauly K, Tierney TS, Hayes MT, Cosgrove GR, Yamaguchi T, Abe K, Taira T, Chang JW. A randomized trial of focused ultrasound thalamotomy for essential tremor. N Engl J Med 2016;375:730–739.

Fan Z, Liu H, Mayer M, Deng CCX. Spatiotemporally controlled single cell sonoporation. Proc Natl Acad Sci USA 2012;109:16486–16491.

Ferri M, Bravo JM, Redondo J, Sánchez-Pérez JV. Enhanced numerical method for the design of 3-D-printed holographic acoustic lenses for aberration correction of single-element transcranial focused ultrasound. Ultrasound Med Biol 2018;45:867–884.

Gateau J, Aubry JF, Pernot M, Fink M, Tanter M. Combined passive detection and ultrafast active imaging of cavitation events induced by short pulses of high-intensity ultrasound. IEEE Trans Ultrason Ferroelectr Freq Control 2011;58:517–532.

Gerstenmayer M, Fellah B, Magnin R, Selingue E, Larrat B. Acoustic transmission factor through the rat skull as a function of body mass, frequency and position. Ultrasound Med Biol 2018;44:2336–2344.

Goldwirt L, Canney M, Horodyckid C, Poupon J, Mourah S, Vignot A, Chapelon JY, Carpentier A. Enhanced brain distribution of carboplatin in a primate model after blood−brain barrier disruption using an implantable ultrasound device. Cancer Chemother Pharmacol 2016;77:211–216.

Graham SM, Carlisle R, Choi JJ, Stevenson M, Shah AR, Myers RS, Fisher K, Peregrino M, Seymour L, Coussios CC. Inertial cavitation to non-invasively trigger and monitor intratumoral release of drug from intravenously delivered liposomes. J Control Release 2014;178:101–107.

Grunert P, Darabi K, Espinosa J, Filippi R. Computer-aided navigation in neurosurgery. Neurosurg Rev 2003;26:73–99 discussion 100−101.

Gyöngy M, Coussios CC. Passive cavitation mapping for localization and tracking of bubble dynamics. J Acoust Soc Am 2010;128: EL175–EL180.

Haworth KJ, Mast TD, Radhakrishnan K, Burgess MT, Kopechek JA, Huang SL, McPherson DD, Holland CK. Passive imaging with pulsed ultrasound insonations. J Acoust Soc Am 2012;132:544.

Haworth KJ, Bader KB, Rich KT, Holland CK, Mast TD. Quantitative frequency-domain passive cavitation imaging. IEEE Trans Ultrason Ferroelectr Freq Control 2017;64:177–191.

Heymans SV, Martindale CF, Suler A, Pouliopoulos AN, Dickinson RJ, Choi JJ. Simultaneous ultrasound therapy and monitoring of microbubble-seeded acoustic cavitation using a single-element transducer. IEEE Trans Ultrason Ferroelectr Freq Control 2017;64:1234–1244.

Horodyckid C, Canney M, Vignot A, Boisgard R, Drier A, Huberfeld G, François C, Prigent A, Santin MD, Adam C, Willer JC, Lafon C, Chapelon JY, Carpentier A. Safe long-term repeated disruption of the blood−brain barrier using an implantable ultrasound device: A multiparametric study in a primate model. J Neurosurg 2017;126:1351–1361.

Hynynen K, McDannold N, Vykhodtseva N, Jolesz FA. Noninvasive MR imaging-guided focal opening of the blood−brain barrier in rabbits. Radiology 2001;220:640–646.

Idbaih A, Canney M, Belin L, Desseaux C, Vignot A, Bouchoux G, Asquier N, Law-Ye B, Leclercq D, Bissery A, Rycke De Y, Trosch C, Capelle L, Sanson M, Hoang-Xuan K, Dehais C, Houillier C, Laigle-Donadey F, Mathon B, André A, Lafon C, Chapelon JY, Delattre JY, Carpentier A. Safety and feasibility of repeated and transient blood-brain barrier disruption by pulsed ultrasound in patients with recurrent glioblastoma. Clin Cancer Res 2019; clincanres.3643.2018.

Ilovitsh T, Ilovitsh A, Foiret J, Caskey CF, Kusunose J, Fite BZ, Zhang H, Mahakian LM, Tam S, Butts-Pauly K, Qin S, Ferrara KW. Enhanced microbubble contrast agent oscillation following 250 kHz insonation. Sci Rep 2018;8:16347.

Jones RM, O'Reilly M, Hynynen K. Transcranial passive acoustic mapping with hemispherical sparse arrays using CT-based skull-specific aberration corrections: A simulation study. Phys Med Biol 2013;58:4981–5005.

Jones RM, O'Reilly MA, Hynynen K. Experimental demonstration of passive acoustic imaging in the human skull cavity using CT-based aberration corrections. Med Phys 2015;42:4385–4400.

Jones RM, Deng L, Leung K, McMahon D, O'Reilly MA, Hynynen K. Three-dimensional transcranial microbubble imaging for guiding volumetric ultrasound-mediated blood−brain barrier opening. Theranostics 2018;8:2909–2926.

Kamimura HAS, Wang S, Wu SY, Karakatsani ME, Acosta C, Carneiro AAO, Konofagou EE. Chirp- and random-based coded ultrasonic excitation for localized blood−brain barrier opening. Phys Med Biol 2015;60:7695–7712.

Kamimura HAS, Wang S, Chen H, Wang Q, Aurup C, Acosta C, Antonio AO, Konofagou EE. Focused ultrasound neuromodulation of cortical and subcortical brain structures using 1.9 MHz. Med Phys 2016;43:5730–5735.

Kamimura HA, Flament J, Valette J, Cafarelli A, Aron Badin R, Hantraye P, Larrat B. Feedback control of microbubble cavitation for ultrasound-mediated blood−brain barrier disruption in non-human primates under magnetic resonance guidance. J Cereb Blood Flow Metab 2018; 0271678X1775351.

Karakatsani MEM, Samiotaki GM, Downs ME, Ferrera VP, Konofagou EE. Targeting effects on the volume of the focused ultrasound-induced blood−brain barrier opening in nonhuman primates in vivo. IEEE Trans Ultrason Ferroelectr Freq Control 2017;64:798–810.

Konofagou EE. Optimization of the ultrasound-induced blood−brain barrier opening. Theranostics 2012;2:1223–1237.

Koruk H, El Ghamrawy A, Pouliopoulos AN, Choi JJ. Acoustic particle palpation for measuring tissue elasticity. Appl Phys Lett 2015;107 223701.

Kotopoulis S, Dimcevski G, Gilja OH, Hoem D, Postema M. Treatment of human pancreatic cancer using combined ultrasound, microbubbles, and gemcitabine: A clinical case study. Med Phys 2013;40 072902.

Lazarus C, Pouliopoulos AN, Tinguely M, Garbin V, Choi JJ. Clustering dynamics of microbubbles exposed to low-pressure 1-MHz ultrasound. J Acoust Soc Am 2017;142:3135–3146.

Lipsman N, Schwartz ML, Huang Y, Lee L, Sankar T, Chapman M, Hynynen K, Lozano AM. MR-guided focused ultrasound thalamotomy for essential tremor: A proof-of-concept study. Lancet Neurol 2013;12:462–468.

Lipsman N, Meng Y, Bethune AJ, Huang Y, Lam B, Masellis M, Herrmann N, Heyn C, Aubert I, Boutet A, Smith GS, Hynynen K, Black SE. Blood−brain barrier opening in Alzheimer's disease using MR-guided focused ultrasound. Nat Commun 2018;9:2336.

Maimbourg G, Houdouin A, Deffieux T, Tanter M, Aubry JF. 3D-printed adaptive acoustic lens as a disruptive technology for transcranial ultrasound therapy using single-element transducers. Phys Med Biol 2018;63 025026.

Mainprize T, Lipsman N, Huang Y, Meng Y, Bethune A, Ironside S, Heyn C, Alkins R, Trudeau M, Sahgal A, Perry J, Hynynen K. Blood−brain barrier opening in primary brain tumors with non-invasive MR-guided focused ultrasound: A clinical safety and feasibility study. Sci Rep 2019;9:321.

Marquet F, Tung YS, Teichert T, Ferrera VP, Konofagou EE. Noninvasive, transient and selective blood−brain barrier opening in non-human primates in vivo. PLoS One 2011;6:1–7.

McDannold N, Arvanitis CD, Vykhodtseva N, Livingstone MS. Temporary disruption of the blood−brain barrier by use of ultrasound and microbubbles: Safety and efficacy evaluation in rhesus macaques. Cancer Res 2012;72:3652–3663.

Melde K, Mark AG, Qiu T, Fischer P. Holograms for acoustics. Nature 2016;537:518–522.

Miller DL, Thomas RM. Contrast-agent gas bodies enhance hemolysis induced by lithotripter shock waves and high-intensity focused ultrasound in whole blood. Ultrasound Med Biol 1996;22:1089–1095.

Morse SV, Pouliopoulos AN, Chan TG, Copping MJ, Lin J, Long NJ, Choi JJ. Rapid short-pulse ultrasound delivers drugs uniformly across the murine blood−brain barrier with negligible disruption. Radiology 2019;291:459–466.

O'Reilly MA, Hynynen K. Blood−brain barrier: Real-time feedback-controlled focused ultrasound disruption by using an acoustic emissions-based controller. Radiology 2012;263:96–106.

O'Reilly MA, Huang Y, Hynynen K. The impact of standing wave effects on transcranial focused ultrasound disruption of the blood−-brain barrier in a rat model. Phys Med Biol 2010;55:5251–5267.

O'Reilly MA, Waspe AC, Ganguly M, Hynynen K. Focused-ultrasound disruption of the blood−brain barrier using closely-timed short pulses: Influence of sonication parameters and injection rate. Ultrasound Med Biol 2011;37:587–594.

O'Reilly MA, Jones R, Hynynen K. Three-dimensional transcranial ultrasound imaging of microbubble clouds using a sparse hemispherical array. IEEE Trans Biomed Eng 2014;61:1285–1294.

Patel A, Schoen SJ, Jr, Arvanitis CD. Closed loop spatial and temporal control of cavitation activity with passive acoustic mapping. IEEE Trans Biomed Eng 2019;66:2022–2031.

Pouliopoulos AN. Controlling microbubble dynamics in ultrasound therapy. PhD thesis. : Imperial College London; 2017.

Pouliopoulos AN, Choi JJ. Superharmonic microbubble Doppler effect in ultrasound therapy. Phys Med Biol 2016;61:6154–6171.

Pouliopoulos AN, Bonaccorsi S, Choi JJ. Exploiting flow to control the in vitro spatiotemporal distribution of microbubble-seeded acoustic cavitation activity in ultrasound therapy. Phys Med Biol 2014;59:6941–6957.

Pouliopoulos AN, Li C, Tinguely M, Garbin V, Tang MX, Choi JJ. Rapid short-pulse sequences enhance the spatiotemporal uniformity of acoustically driven microbubble activity during flow conditions. J Acoust Soc Am 2016;140:2469–2480.

Pouliopoulos A, Smith C, El Ghamrawy A, Tang M, Choi J. Doppler passive acoustic mapping for monitoring microbubble velocities in ultrasound therapy. J Acoust Soc Am 2017;141 3491−3491.

Pouliopoulos AN, Burgess MT, Konofagou EE. Pulse inversion enhances the passive mapping of microbubble-based ultrasound therapy. Appl Phys Lett 2018;113 044102.

Salgaonkar VA, Datta S, Holland CK, Mast TD. Passive cavitation imaging with ultrasound arrays. J Acoust Soc Am 2009;126:3071–3083.

Shamout FE, Pouliopoulos AN, Lee P, Bonaccorsi S, Towhidi L, Krams R, Choi JJ. Enhancement of non-invasive trans-membrane drug delivery using ultrasound and microbubbles during physiologically relevant flow. Ultrasound Med Biol 2015;41:2435–2448.

Sheikov N, McDannold N, Sharma S, Hynynen K. Effect of focused ultrasound applied with an ultrasound contrast agent on the tight junctional integrity of the brain microvascular endothelium. Ultrasound Med Biol 2008;34:1093–1104.

Sun T, Zhang Y, Power C, Alexander PM, Sutton JT, Aryal M, Vykhodtseva N, Miller EL, McDannold NJ. Closed-loop control of targeted ultrasound drug delivery across the blood-brain/tumor barriers in a rat glioma model. Proc Natl Acad Sci USA 2017;114:E10281–E10290.

Treeby BE, Cox BT. k-Wave: MATLAB toolbox for the simulation and reconstruction of photoacoustic wave fields. J Biomed Opt 2010;15 021314.

Treeby BE, Jaros J, Rendell AP, Cox BT. Modeling nonlinear ultrasound propagation in heterogeneous media with power law absorption using a *k*-space pseudospectral method. J Acoust Soc Am 2012;131:4324–4336.

Tung YS, Vlachos F, Choi JJ, Deffieux T, Selert K, Konofagou EE. In vivo transcranial cavitation threshold detection during ultrasound-induced blood-brain barrier opening in mice. Phys Med Biol 2010;55:6141–6155.

Tyler WJ, Lani SW, Hwang GM. Ultrasonic modulation of neural circuit activity. Curr Opin Neurobiol 2018;50:222–231.

Wei KC, Tsai HC, Lu YJ, Yang HW, Hua MY, Wu MF, Chen PY, Huang CY, Yen TC, Liu HL. Neuronavigation-guided focused ultrasound-induced blood−brain barrier opening: A preliminary study in swine. AJNR Am J Neuroradiol 2013;34: 115–120.

Wu SY, Aurup C, Sanchez CS, Grondin J, Zheng W, Kamimura H, Ferrera VP, Konofagou EE. Efficient blood−brain barrier opening in primates with neuronavigation-guided ultrasound and real-time acoustic mapping. Sci Rep 2018;8:7978.

Xia JZ, Xie FL, Ran LF, Xie XP, Fan YM, Wu F. High-intensity focused ultrasound tumor ablation activates autologous tumor-specific cytotoxic T lymphocytes. Ultrasound Med Biol 2012;38:1363–1371.